CHEMIJA
2026. Vol. 37. No. 3. P. 194–205

ISSN 0235-7216 eISSN 2424-4538
DOI: https://doi.org/10.6001/chemija.2026.37.3.2

Electrochemical detection of ibuprofen at a graphene–chitosan modified glassy carbon electrode: Integrating differential pulse voltammetry with machine learning calibration

Islam Hassan[1, 2],

Mohamed Abdelkader[1*],

Rasa Pauliukaitė[1, 2]

[1] *Department of Nanoengineering, Center for Physical Sciences and Technology (FTMC), 231 Savanorių Street, 02300 Vilnius, Lithuania*

[2] *Institute of Chemistry, Faculty of Chemistry and Geosciences, Vilnius University, 24 Naugarduko Street, 03225 Vilnius, Lithuania*

A graphene–chitosan modified glassy carbon electrode (Gr-Chit/GCE) was evaluated for the differential pulse voltammetric (DPV) determination of ibuprofen (IBF) and paired with a transparent machine learning (ML) calibration audit. In a 0.1 M phosphate-based electrolyte (PBE, pH 7.5), the modified electrode gave a linear DPV response from 100 to 488 μmol/L after background subtraction, following $I_p = 0.0828 + 0.0275C$ ($R^2 = 0.9970$). The recalculated limit of detection (LOD) and the limit of quantification (LOQ) were 22.27 and 74.25 μM, respectively. Cyclic voltammetric characterisation with $[Fe(CN)_6]^{3-/4-}$ showed a diffusion-controlled behaviour and a 4.2-fold increase in the electroactive surface area after Gr-Chit deposition. Interference tests indicated that ascorbic acid was resolved at lower potential, while acetaminophen contributed in the IBF potential region without masking the analyte response. The leave-one-out cross-validation of six calibration models showed that the ordinary least-squares inverse calibration gave the lowest prediction error (root-mean-square error, RMSE = 12.11 μmol/L), whereas more complex nonlinear models showed a poorer generalisation for the five-point calibration set. The study therefore positions ML not as a black-box replacement for electroanalytical calibration, but as an auditable model-selection layer for small voltammetric datasets.

Keywords: ibuprofen, differential pulse voltammetry, graphene–chitosan, glassy carbon electrode, machine learning, electrochemical sensor, NSAID, cyclic voltammetry

INTRODUCTION

Ibuprofen (IBF), 2-(4-isobutylphenyl)propionic acid, is one of the most widely used non-steroidal anti-inflammatory drugs (NSAIDs) for pain, fever, and inflammatory conditions [1, 2]. Its broad use, an incomplete metabolism and an improper disposal contribute to the occurrence of IBF and related residues in wastewater effluents, surface waters and drinking-water sources [3, 4]. These environmental and public-health concerns create demand for analytical methods that are rapid, inexpensive and sufficiently robust for decentralised monitoring [3, 5].

Conventional analytical techniques for IBF detection, such as high-performance liquid chromatography (HPLC), gas chromatography–mass spectrometry (GC-MS) and capillary electrophoresis,

* Corresponding author. Email: mohamed.fawzy@mena.vt.edu

offer a high sensitivity and selectivity but require an expensive instrumentation, trained personnel, and a lengthy sample preparation, and are not well-suited for on-site or real-time monitoring [6]. While HPLC-UV and LC-MS/MS remain gold standards for pharmaceutical analysis, their inherent complexity makes them impractical for decentralised or field-based scenarios.

Electrochemical methods offer an attractive alternative owing to their inherent advantages of a high sensitivity, a rapid response, a low cost, portability, and the possibility of miniaturisation [7]. Among electrochemical techniques, differential pulse voltammetry (DPV) is particularly suited for trace-level quantification because it effectively separates faradaic current from capacitive background, yielding higher signal-to-noise ratios. DPV achieves this by applying a series of small-amplitude potential pulses and recording the current difference at the beginning and end of each pulse; this suppresses the fast-decaying capacitive component while isolating the slower faradaic response [8].

The choice of a working electrode largely determines the sensitivity, stability, and the usable potential window of an electrochemical sensor. Glassy carbon electrodes (GCEs) are frequently selected for voltammetric analysis because they combine chemical robustness, a good conductivity, a low background current, and a convenient surface renewal [9]. These features make GCEs suitable for cyclic voltammetry (CV), DPV, and square-wave voltammetry (SWV) measurements in both qualitative and quantitative workflows. At the same time, an unmodified GCE can show a limited active-site density and a slower interfacial electron transfer, particularly when oxidation products adsorb on the carbon surface. Such fouling may lower sensitivity and reproducibility during repeated measurements [7, 10, 11].

Several pretreatment strategies have been used to improve the response of bare GCE surfaces. For example, anodic polarisation can generate oxygen-containing surface groups that increase electrochemical activity without major morphological changes [12]. However, surface activation alone may not provide a sufficient analytical performance for trace IBF determination. This limitation supports the use of nanostructured modifiers that increase an accessible area and facilitate charge transfer [13].

Graphene (Gr), a two-dimensional carbon allotrope consisting of sp^2-hybridised carbon atoms arranged in a hexagonal lattice, has emerged as a transformative material in electrochemical sensing due to its extraordinary electrical conductivity (~10^4 S/cm), a large theoretical surface area (2630 m^2/g), an excellent mechanical flexibility, and a broad electrochemical potential window [14]. When combined with chitosan (Chit), a naturally derived biopolymer obtained by deacetylation of chitin, the resulting graphene–chitosan (Gr-Chit) nanocomposite offers synergistic advantages [14, 15]. Chit offers biocompatibility, excellent film-forming properties, and abundant amino and hydroxyl functional groups that facilitate the uniform dispersion of Gr sheets, preventing irreversible aggregation via π–π stacking. The recent work has further demonstrated that Chit can suppress electrode polarisation in graphene oxide (GrO)-based films, thereby enabling more stable and reproducible electrochemical responses [16].

The Gr-Chit composite has been successfully employed for the electrochemical determination of various analytes, including tyrosine, dopamine, ascorbic acid (AA) and uric acid [17]. Luo and Li demonstrated that Gr-Chit/GCE exhibited enhanced electrocatalytic activity toward tyrosine oxidation, with a limit of detection (LOD) of 0.5 μM attributed to the large electroactive surface area and facilitated electron transfer at the nanocomposite interface [17, 18]. In the context of NSAID detection, a recent review of electrochemical sensors for IBF and ketoprofen highlighted that modified electrodes, particularly GCE-based platforms, exhibit an enhanced sensitivity and analytical performance for NSAID detection [4].

The electrochemical oxidation of IBF is electrode-dependent [19, 20]. At conventional electrodes such as GCE, IBF oxidation generally proceeds through an irreversible, diffusion-controlled, single-electron process and exhibits a pH-independent behaviour above pH 7.5 [19], as illustrated in Fig. 1. The process involves electron/proton transfer from the isobutylphenyl moiety. The enhanced response at Gr-Chit/GCE is attributed to the synergistic modifier effect: Gr provides efficient electron-transfer pathways through edge-plane defect sites and an extended pi-conjugated network, while Chit promotes film integrity, dispersion stability, and surface homogeneity.

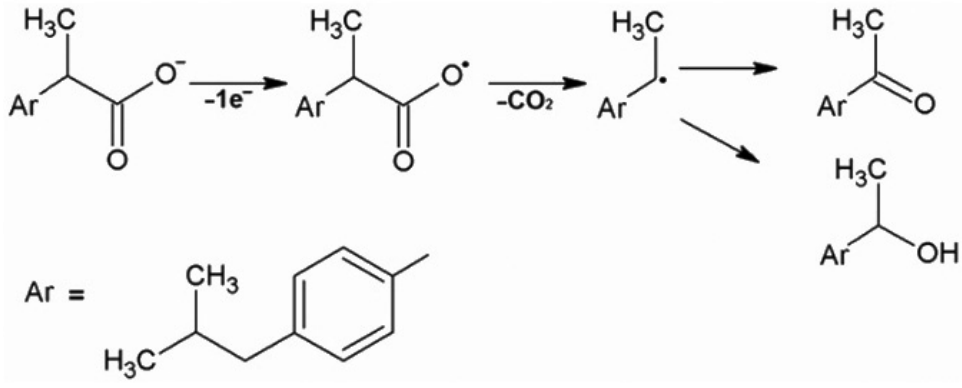

Fig. 1. Proposed oxidation pathway of ibuprofen at GCE in 0.1 M PBE and 0.1 M Britton–Robinson (BR) buffer (separate experiments). The pH-independent response over pH 7.5–12 and the calculated electron number (approximately 0.92) support an overall one-electron oxidation process. Adapted from Ref. [19]

Alongside electrode engineering, machine learning (ML) is increasingly used in electrochemical analysis to assist calibration, automate data interpretation, and exploit multivariate voltammetric information [21]. For a simple peak current calibration, however, model complexity must be justified rather than assumed. Linear calibration remains appropriate when the current–concentration relationship is near linear, while nonlinear approaches become useful mainly when matrix effects, drift, overlapping signals, or multifeature responses carry additional information. Recent ML-guided electrochemical sensing studies illustrate this potential in richer datasets [22, 23].

For small electrochemical calibration sets, the key editorial question is not whether ML can be applied, but whether it improves prediction without overfitting. Small-n validation is sensitive to model flexibility, feature-to-sample ratio, and leakage caused by preprocessing outside the validation loop [24, 25]. This study therefore treats ML as a validation framework: classical inverse calibration and lightweight nonlinear models are tested under the same leave-one-out design to determine whether added complexity improves concentration prediction for IBF.

The work first establishes the electrochemical behaviour of Gr-Chit/GCE by CV with $[Fe(CN)_6]^{3-/4-}$, including the electroactive surface area, scan-rate dependence and kinetic interpretation. It then evaluates the DPV detection of IBF through the calibration figures of merit, selectivity tests in buffer and tap water, and the comparison with selected electrochemical IBF sensors.

The ML component is then integrated into the analytical discussion rather than treated as a separate novelty claim. Six models were compared by leave-one-out cross-validation: ordinary least-squares inverse calibration, ridge regression, polynomial regression, bagged regression stumps, gradient-boosted stumps, and radial-basis-function kernel ridge regression. The central test was whether these alternatives improve prediction beyond the simplest defensible linear model.

THEORETICAL BACKGROUND

Differential pulse voltammetry

DPV is a highly sensitive electroanalytical technique in which the applied potential consists of a staircase waveform superimposed with fixed-amplitude pulses [7, 8]. Current is sampled just before each pulse and at the end of each pulse; the difference (ΔI) is recorded as a function of the staircase potential. This differential approach cancels the capacitive (non-faradaic) background current, which decays rapidly after potential application, while preserving the slower-decaying faradaic current arising from analyte oxidation or reduction at the electrode surface. The result is a peak-shaped voltammogram whose peak current (I_p) is proportional to the analyte concentration and whose peak potential (E_p) provides the qualitative identification of the redox species.

For an irreversible electrochemical oxidation (such as IBF), the DPV peak current scales as $I_p \propto (nFAD^{1/2} c)/(\pi^{1/2} t_p^{1/2}) \times (1 - \sigma)/(1 + \sigma)$, where n is the number of electrons transferred, F is the Faraday constant, A is the electrode area, D is the diffusion coefficient, c is the bulk analyte concentration, t_p is the pulse width, and $\sigma = \exp(nF\Delta E/2RT)$ with ΔE, the pulse amplitude [7]. For small pulse amplitudes ($\Delta E \ll RT/nF$), the signal scales linearly with concentration, forming the basis of quantitative calibration. The linear concentration–current relationship, combined with DPV's inherent background rejection, makes it one of the most sensitive voltammetric techniques for the analysis of pharmaceutical trace levels.

Electroactive surface area and the Randles–Ševčík equation

The electroactive surface area of an electrode is a critical parameter that influences analytical sensitivity. For a reversible or quasi-reversible redox process under diffusion-controlled conditions at 25°C, the peak current scales with the square root of the scan rate according to the Randles–Ševčík equation [26]:

$$I_p = 2.69 \times 10^5 \cdot n^{3/2} \cdot A \cdot D^{1/2} \cdot C \cdot \nu^{1/2}. \quad (1)$$

In Eq. 1, I_p denotes the peak current in amperes, n is the number of electrons involved in the $[Fe(CN)_6]^{3-/4-}$ redox process ($n = 1$), A is the electroactive surface area in cm^2, D is the ferricyanide diffusion coefficient (7.6×10^{-6} cm^2/s in 0.1 M electrolyte), c is the bulk concentration in mol/cm^3, and ν is the scan rate in V/s. The slope of I_p plotted against $\nu^{1/2}$ therefore provides A [26]. Comparing A with the geometric electrode area gives the roughness factor. The values below unity are typical of a polished, relatively smooth surface, whereas Gr-Chit modification introduces additional edge sites, functional groups and porous pathways that increase the active area available for electron transfer.

Electron transfer kinetics: log–log analysis and Laviron formalism

The mechanistic origin of the electrode process is diagnosed by the power-law dependence of peak current on the scan rate [7]:

$$\log I_p = b \cdot \log \nu + \log a. \quad (2)$$

A slope $b = 0.5$ is diagnostic of a purely diffusion-controlled process governed by semi-infinite linear diffusion, whereas $b = 1.0$ indicates a surface-confined (adsorption-controlled) process. Intermediate values suggest mixed mechanisms. This diagnostic is crucial for understanding whether the analytical signal at the Gr-Chit/GCE arises from solution-phase IBF diffusing to the surface or from surface-adsorbed IBF.

For quasi-reversible electron-transfer kinetics, the Laviron model describes the dependence of the peak potential on the scan rate [8]. For an irreversible or quasi-reversible process, the anodic peak potential shifts with the scan rate according to

$$E_p = E^{o\prime} + (RT/(\alpha nF)) \ln((RTk_s)/(\alpha nF\nu)), \quad (3)$$

where $E^{o'}$ is the formal potential, α is the transfer coefficient, k_s is the standard heterogeneous electron-transfer rate constant, R is the universal gas constant (8.314 J mol^{-1} K^{-1}), T is the absolute temperature (298 K), n is the number of electrons, and F is the Faraday constant (96485 C mol^{-1}). A linear plot of E_p versus ln(ν) confirms a quasi-reversible behaviour and allows the extraction of α and k_s. The observation of an increasing peak-to-peak separation (ΔE_p) with an increasing scan rate, which deviates from the ideal 59/n mV for a fully reversible system, further corroborates quasi-reversible kinetics [7].

EXPERIMENTAL

Materials and reagents

IBF (≥98%), few-layer Gr nanoplatelets (average lateral size approximately 8 μm), low-molecular-weight Chit (degree of deacetylation ≥75%), $K_3[Fe(CN)_6]$, $K_4[Fe(CN)_6]\cdot 3H_2O$, NaCl, KCl, H_3PO_4, Na_2HPO_4 and H_3BO_3 were supplied by Sigma-Aldrich; no further purification was applied. The 0.1 M phosphate-based electrolyte (PBE) at pH 7.5 was prepared from the corresponding phosphate components and adjusted with NaOH.

For the interference experiments, AA and acetaminophen (ACT) (≥98%, Sigma-Aldrich) were chosen as model species likely to contribute voltammetric signals near pharmaceuticals.

Individual 20 mM stocks were made in 0.1 M PBE at pH 7.5, and working mixtures were prepared by dilution in the appropriate test medium.

Chitosan solution (0.5%, w/v) was made in dilute acetic acid (1%, v/v) by stirring until clear. For the modifier ink, 1.5 mg of Gr nanoplatelets was introduced into a 1.0 mL portion of this chitosan vehicle, and the mixture was treated in an ultrasonic bath for 2 h before casting.

Water used for solution preparation was deionised to a resistivity of at least 18.2 MΩ·cm.

Electrode preparation

The working surface was renewed before use. 3 mm GCE (geometric area 0.071 cm^2) was polished sequentially with 1.0, 0.3 and 0.05 μm alumina suspensions, washed, ultrasonically cleaned in ethanol and water for 60 s each, and conditioned by 20 CV cycles in 0.1 M KCl from –1.0 to +1.0 V at 0.10 V/s.

The modifier film was formed by placing 5 μL of freshly sonicated Gr-Chit ink on the cleaned GCE. The coated electrode was left to dry overnight at room temperature and was briefly rinsed with deionised water before electrochemical measurements.

Electrochemical measurements

All electrochemical measurements were performed using a conventional three-electrode system with the modified or bare GCE as the working electrode, a platinum wire as the counter electrode, and an Ag/AgCl (3 M KCl internal filling) reference electrode. Measurements were carried out at room temperature. All potentials are reported versus Ag/AgCl.

Differential pulse voltammetry

DPV experiments used the Gr-Chit/GCE in 0.1 M PBE (pH 7.5). Scans covered +0.5 to +1.6 V vs Ag/AgCl at 20 mV/s; pulse amplitude, pulse width and step potential were 50 mV, 0.05 s and 5 mV, respectively. The calibration series contained a blank electrolyte and 100, 198, 296, 396 and 488 μM IBF. For each concentration, the blank trace was subtracted from the recorded DPV curve so that the plotted response represented the IBF faradaic current.

Cyclic voltammetry

CV characterisation was performed on the bare GCE in a solution of 1 mM $[Fe(CN)_6]^{3-/4-}$ in 0.1 M NaCl. The potential was swept from –0.15 to +1.0 V vs Ag/AgCl at scan rates of 10, 30, 50, 75, 100, 120, 150 and 200 mV/s. These measurements were used to determine the electroactive surface area, assess the electrode process (diffusion vs adsorption control), and evaluate the kinetic regime using Laviron analysis.

Data analysis and machine learning framework

Data processing, calibration, and ML analysis were carried out in Python 3.11 using NumPy, pandas, openpyxl and Pillow. Calibration data were imported from the experimental workbook, and comma-decimal artifacts were corrected before modelling (for example, 2997 was read as 2.997 μA). Classical figures of merit were calculated from the peak-current/concentration relationship. The machine-learning model set, its hyperparameters, validation and results are reported together in Section 'Machine-learning-assisted calibration'.

RESULTS AND DISCUSSION

Electrode characterisation

The electrode surfaces were first compared by CV in 1 mM $[Fe(CN)_6]^{3-/4-}$ prepared in 0.1 M NaCl. Figures 2a and 2b show the scan-rate series for the bare GCE and Gr-Chit/GCE, recorded from –0.15 to +1.0 V vs Ag/AgCl over 10–200 mV s^{-1}.

Both electrodes gave quasi-reversible ferri/ferrocyanide responses. In the inset plots, the peak current scaled linearly with $\nu^{1/2}$, showing that diffusion was the dominant transport mode.

At 50 mV s^{-1}, the Gr-Chit coating increased both anodic and cathodic currents relative to the unmodified GCE (Fig. 2c), consistent with a more accessible conductive surface after film deposition.

Using the Randles–Ševčík expression (Eq. 1), electroactive surface area values were obtained from the I_p-versus-$\nu^{1/2}$ slopes for the reversible diffusion-controlled probe at 25°C [12, 27]. The bare GCE gave 0.048 cm^2, whereas the Gr-Chit/GCE gave 0.205 cm^2; the corresponding roughness factors were 0.68 and 2.89. The coating therefore increased the effective active area by approximately 4.2-fold.

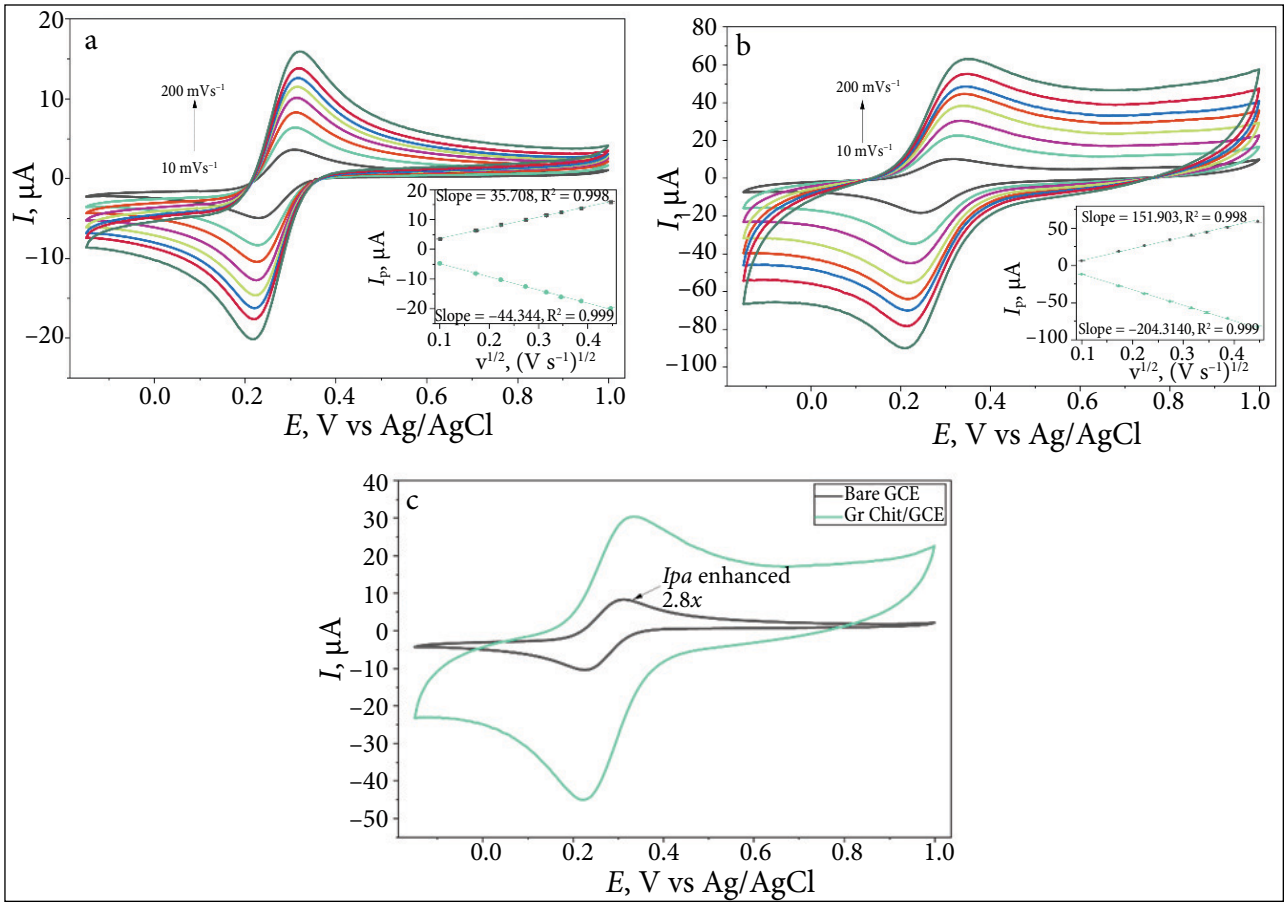

Fig. 2. Scan-rate-dependent CVs of 1 mM $[Fe(CN)_6]^{3-/4-}$ in 0.1 M NaCl at (a) bare GCE and (b) Gr-Chit/GCE over 10–200 mV s^{-1}. Insets show the diffusion-controlled I_p–$v^{1/2}$ relationships. (c) CV comparison of bare and modified electrodes at 50 mV s^{-1}

DPV detection of IBF

DPV was used to evaluate whether the Gr-Chit coating translated the surface-area gain into a useful IBF signal. The bare GCE gave measurable oxidation only at the higher concentration interval of 952–2222 µM, whereas the Gr-Chit/GCE produced a resolved analytical response from 100 to 488 µM (Fig. 3a, b). The oxidation maximum shifted from +1.195 to +1.275 V on bare GCE to +1.162 to +1.230 V on Gr-Chit/GCE, supporting a lower overpotential at the modified interface.

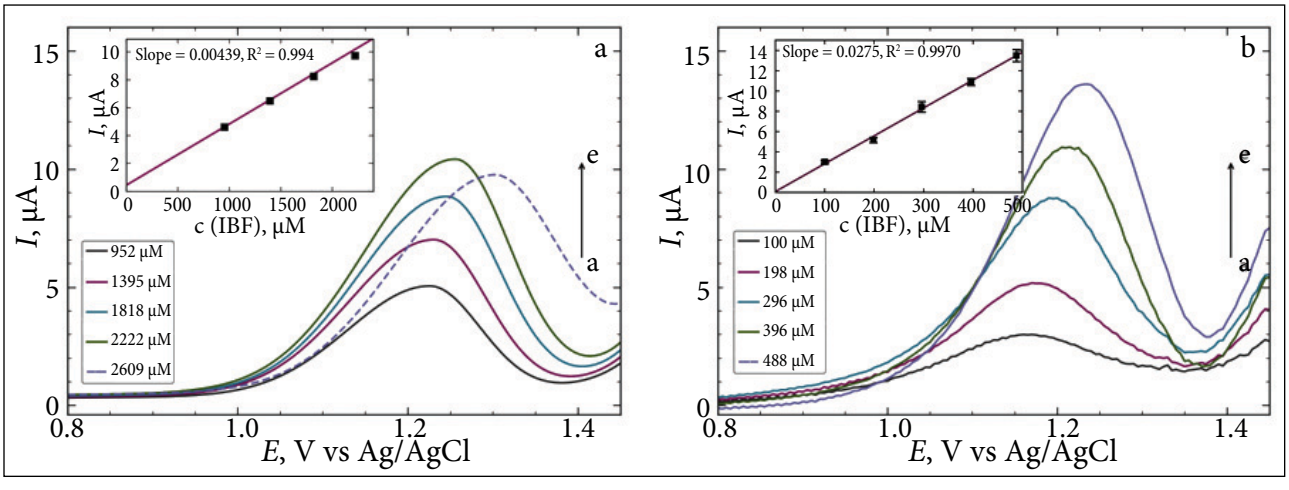

Fig. 3. DPVs of IBF recorded at (a) bare GCE and (b) Gr-Chit/GCE in 0.1 M PBE (pH 7.5), after baseline subtraction. Insets show the corresponding calibration curves

At the upper end of the bare-GCE series, peak definition deteriorated. This loss of response is attributed to the passivation of the carbon surface by adsorbed IBF oxidation products, which reduces access to active sites during high-concentration measurements.

The modified electrode also showed a better signal stability within the tested concentration range. Graphene provides conductive pathways and defect-rich sites, while chitosan improves film integrity and dispersion retention; together these features plausibly reduce passivation and improve charge transfer. The Gr-Chit/GCE calibration gave R^2 = 0.9970, sensitivity = 0.0275 μA $μM^{-1}$, LOD = 22.27 μM, and limit of quantification (LOQ) = 74.25 μM, compared with a LOD of 168.51 μM for the bare GCE. Calibration points in the inset of Fig. 3b are the mean values of three measurements performed with independently prepared electrodes (n = 3); error bars represent ± one standard deviation (RSD ≤ 6.2%). The main contribution is therefore not ultratrace sensitivity, but a simple and reproducible electrode modification that lowers the practical IBF detection range. This positioning is important when compared with the aptamer-, quantum-dot- and nanoparticle-based platforms summarised in Table 2.

Reproducibility was evaluated using three independently prepared Gr-Chit/GCE electrodes. Each electrode was fabricated following the same procedure and used to record the calibration response. The calculated relative standard deviations (RSDs) were 4.98, 5.00, 6.18, 3.17 and 4.39% for 100, 198, 296, 396 and 488 μM IBF, respectively, indicating the acceptable analytical precision for the Gr-Chit/GCE platform. The corresponding standard deviations (n = 3) are shown as error bars in the Gr-Chit/GCE calibration plots (inset of Figs 3b and 5a).

Table 1. **Analytical performance parameters for IBF detection at bare GCE and Gr-Chit/GCE, including linear range, sensitivity, LOD and LOQ**

Electrode	Linear range, μM	Sensitivity, μA $μM^{-1}$	LOD, μM	LOQ, μM
Bare GCE	952–2222	0.0044	168.5	622.8
Gr-Chit/GCE	100–488	0.0275	22.27	74.25

Table 2. **Selected electrochemical methods for IBF determination, including the present Gr-Chit/GCE platform**

Sensor electrode	Method	Electrolyte	Sample matrix	LOD	Linear range	Ref.
SD-MWCNTs/GCE	CA	0.1 M PB, pH 7.5	Pharmaceuticals	1.9 μM	10–1000 μM	[19]
Screen-printed graphite electrode	SWV	0.25 M acetate buffer, pH 4.7	Surface water	6.3 μM	10–50 μM	[28]
Gr/PTh/GCE	DPV	0.1 M PBS, pH 7.1	Pharmaceuticals; biological samples	1.24 μM	10–80 μM	[27]
NDCNDs/CoTAPhPcNPs/GCE	DPV	0.1 M PBS, pH 5.5	Wastewater	4.19 nM	Not reported	[29]
MB/Apt/MWCNTs/IL/Chitosan/GCE	DPV	0.1 M PBS, pH 7.4	Pharmaceuticals; blood serum; wastewater	20 pM	70 pM–6 μM	[30]
Apt/Den/CdTe QD/GCE	DPV	0.1 M PB, pH 7.4	Blood serum	333 fM	0.001–12 nM	[31]
Apt/CdTeQD/GCE	EIS	5 mM $[Fe(CN)_6]^{3-/4-}$ + 0.5 M KCl	Pharmaceuticals; blood serum	16 pM	0.05–20,000 nM	[32]
Apt/AuNPs@N-GQDs/GCE	DPV	0.1 M PB, pH 7.4	Pharmaceuticals; blood serum; wastewater	33.33 aM	1.0×10^{-7}–200 nM	[33]
Gr-Chit/GCE	DPV	0.1 M PBE, pH 7.5	Buffer; tap-water test	22.27 μM	100–488 μM	This work

Apt, aptamer; AuNPs, gold nanoparticles; CA, chronoamperometry; CdTeQD, cadmium telluride quantum dot; Chit, chitosan; CoTAPhPcNPs, cobalt tetraaminophenoxy phthalocyanine nanoparticles; Den, dendrimer; DPV, differential pulse voltammetry; EIS, electrochemical impedance spectroscopy; GCE/GC, glassy carbon electrode/glassy carbon; Gr, graphene; IL, ionic liquid; MB, methylene blue; MWCNTs, multi-walled carbon nanotubes; NDCNDs, nitrogen-doped carbon nanodots; N-GQDs, nitrogen-doped graphene quantum dots; PB, phosphate buffer; PBE, phosphate-based electrolyte; PBS, phosphate-buffered saline; PTh, polythiophene; QDs, quantum dots; SD, shorter dimension; SWV, square-wave voltammetry.

Operational stability was evaluated by repeated DPV measurements on a single Gr-Chit/GCE immersed in a static 296 μM IBF solution. The electrode remained in the solution for the entire 330 min experiment, and a full DPV scan was recorded every 10 min using the same pulse parameters as in the calibration. For each scan, the IBF peak current was extracted from the baseline-subtracted voltammogram. This procedure allowed the temporal evolution of the peak current to be monitored under continuous exposure without removing or re-polishing the electrode. The current decreased from 8.47 to 8.02 μA during this time period, corresponding to a 5.31% change over the measurement period. Although a gradual decrease was observed, the IBF peak remained clearly measurable throughout the experiment. These results show that the signal can be monitored over 330 min under the conditions tested, without implying stability beyond this timeframe.

Selectivity and interference study

Interference was tested with AA and ACT because both can contribute oxidation currents in the samples that contain pharmaceuticals. Experiments were run in 0.1 M PBE (pH 7.5) and in tap water (about pH 7.4), giving one controlled buffer medium and one simple real-water matrix. Equal-ratio mixtures were prepared from 20 mM stocks of IBF, AA and ACT.

With 296 μM IBF in PBE, adding equimolar AA and ACT did not remove the IBF feature (Fig. 4a). AA produced a separate peak at lower potential, so it was distinguishable from IBF. ACT, however, oxidised in the IBF region; the mixed ACT/IBF band therefore increased the apparent current rather than decreasing the analyte response.

Tap water led to the same practical conclusion (Fig. 4b). Extra ions in the matrix did not change the interpretation or the recognisable IBF response: the peak remained visible and broadly comparable to the buffer measurement despite the more complex background.

Matrix effects were evaluated by comparing the IBF response in tap water with that obtained in PBE at the same concentration (296 μM). The peak current in tap water was 1.94 μA, substantially lower than the corresponding value in PBE (8.45 μA), representing a 77.0% decrease in signal intensity (Fig. 4b). The voltammogram also showed a broader peak shape and a higher background current at positive potentials. These observations indicate that the tap-water matrix introduces a pronounced effect on the IBF response. Although the IBF peak remained detectable, the reduced signal indicates that matrix-specific calibration or standard-addition methods are required for the quantitative analysis of real-water samples.

These data should not be overread as complete selectivity. ACT remains a co-oxidising species near the IBF potential, so confirmatory work would be needed for heavily contaminated matrices. The useful point is narrower: under the 1:1:1 challenge, AA is resolved, and the ACT overlap is additive rather than masking, allowing IBF to remain identifiable.

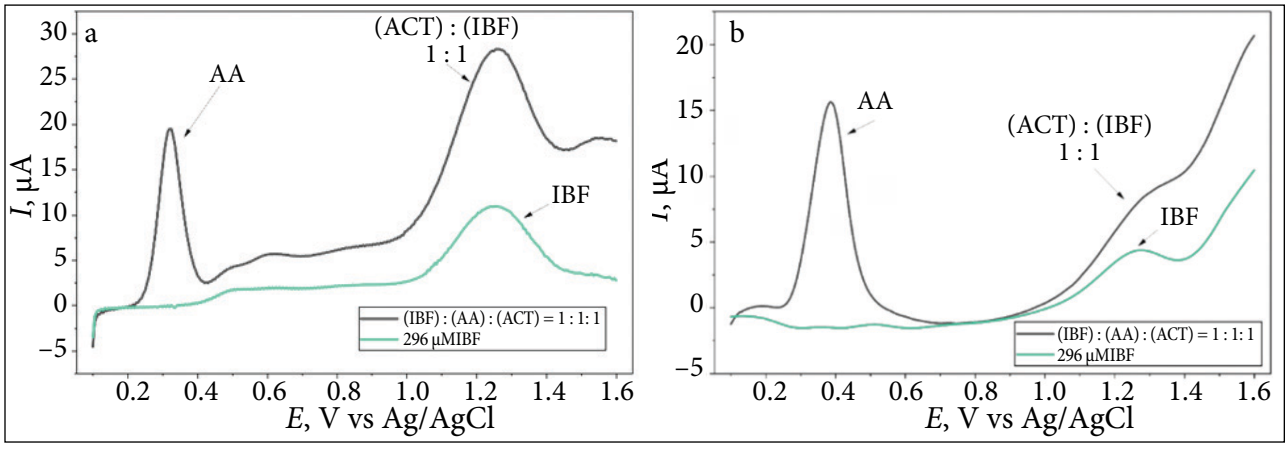

Fig. 4. DPV selectivity test for 296 μM IBF at the Gr-Chit/GCE in (a) 0.1 M PBE (pH 7.5) and (b) tap water (pH ≈ 7.4). Measurements compare IBF alone with equimolar IBF, AA and ACT mixtures (1:1:1)

For screening-type applications, this behaviour is adequate for simple aqueous samples where a minimal pretreatment is desirable. The sensor discriminates best when interferents appear at lower potentials and is more limited when compounds oxidise in the IBF window.

Overall, the interference study supports the use of Gr-Chit/GCE as a practical IBF screening electrode in buffer and tap-water matrices, while making clear that complex samples would still require validation against matrix-specific interferents.

Machine-learning-assisted calibration

Classical voltammetric calibration uses ordinary least-squares (OLS) linear regression to relate peak current to concentration; this is optimal when the signal is linear in concentration, the errors are homoscedastic and normally distributed, and the dataset is small relative to model complexity [21]. Ridge regression adds an L2 penalty ($\lambda\Sigma\beta_i^2$) that shrinks the coefficients and reduces variance at the cost of a small bias; in well-conditioned, low-dimensional problems, it converges to OLS and offers no practical advantage. Nonlinear ensemble methods (random forests, gradient boosting) and kernel methods (support-vector and kernel-ridge regression with radial-basis-function (RBF) kernels) can capture complex concentration–response relationships [22, 23], but they carry many learnable parameters and overfit when training data are scarce: complex models have a low bias but a high variance, whereas simple linear models have a higher bias but a lower variance and generalise better from few observations [21, 25].

To test whether any data-driven model improves on classical calibration, six models were compared using peak current as the single predictor and IBF concentration as the response: OLS inverse calibration, ridge regression (alpha = 1), polynomial regression (degree = 2), bagged regression stumps, gradient-boosted stumps, and RBF kernel-ridge regression. All models were implemented in Python 3.11 (scikit-learn) and assessed by leave-one-out cross-validation (LOO-CV), in which each of the five points is held out once while the others are used for fitting; preprocessing was performed within each fold to avoid data leakage, and performance was reported as R^2, root-mean-square error (RMSE), and mean absolute error (MAE) for the held-out concentration predictions [24, 25]. Because $n = 5$, LOO-CV is treated here as a transparent validation exercise rather than as evidence that nonlinear models are intrinsically superior.

The ML analysis was restricted to the five non-zero Gr-Chit/GCE calibration points because they define the analytically relevant low-concentration interval of the modified sensor. The corrected pairs were 100, 198, 296, 396 and 488 μM IBF with peak currents of 2.997, 5.163, 8.450, 10.906 and 13.507 μA, respectively. The ordinary current-versus-concentration calibration was $I_p = 0.0828 + 0.0275C$, where I_p is in μA and C is in μmol/L ($R^2 = 0.9970$). Using the low-level current-noise estimate of 0.204 μA, the recalculated LOD and LOQ were 22.27 and 74.25 μmol/L.

The leave-one-out cross-validation showed that the OLS inverse calibration generalised best; RMSE and MAE were 12.11 and 9.76 μmol/L, respectively. Polynomial regression remained acceptable, but ridge regression and nonlinear tree/kernel models produced larger held-out errors. This outcome is chemically and statistically reasonable: the DPV response is near linear, and the calibration set is too small to support flexible models. The ML contribution is therefore

Table 3. **Leave-one-out cross-validation performance for the IBF concentration prediction from the DPV peak current**

Model	R^2	RMSE, μM	MAE, μM
OLS linear	0.992	12.11	9.76
Ridge regression	0.926	37.47	30.99
Polynomial degree 2	0.978	20.27	17.21
Bagged regression stumps	0.360	110.23	97.58
Gradient-boosted stumps	0.495	97.94	97.90
RBF kernel ridge	0.088	131.53	100.77

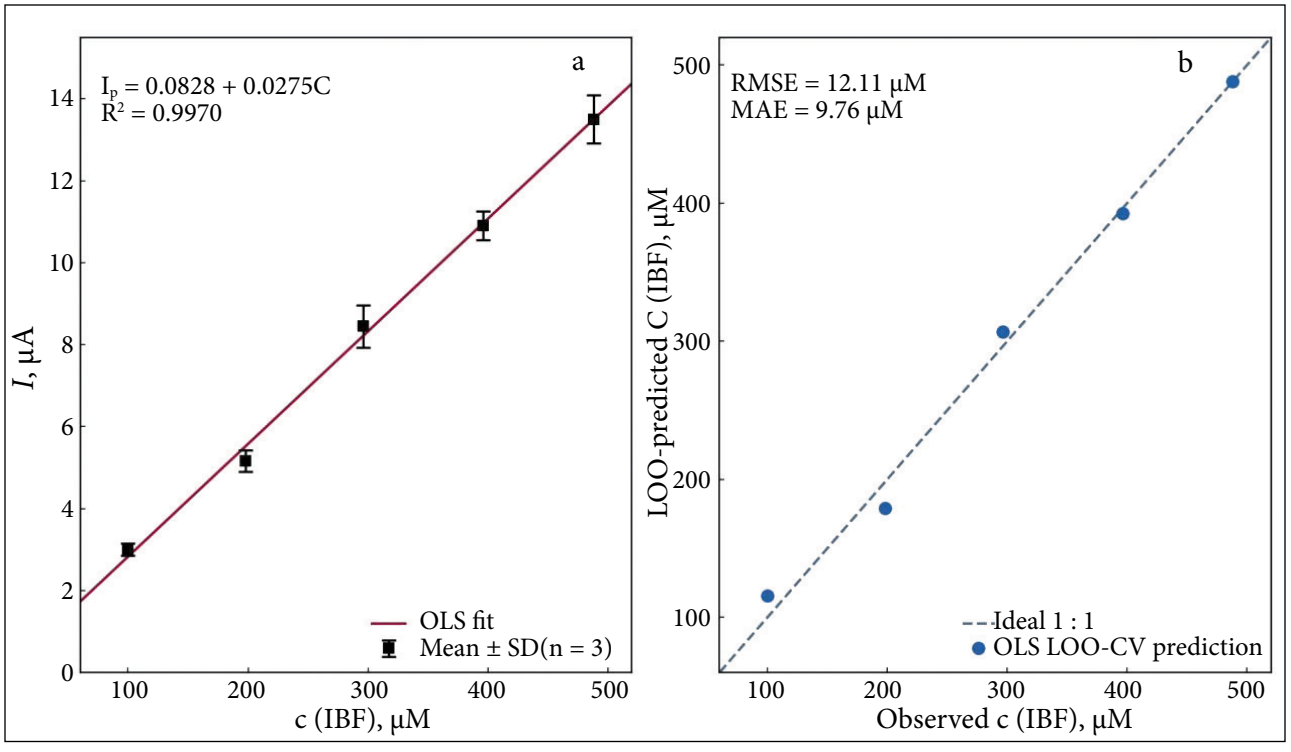

Fig. 5. Machine-learning-assisted calibration of IBF at Gr-Chit/GCE. (a) DPV calibration showing the mean peak current ($n = 3$) as a function of IBF concentration. (b) Leave-one-out cross-validation predictions from the OLS inverse calibration model plotted against the observed concentration

a transparent model-selection audit that confirms the simplest reliable calibration model and documents why more complex alternatives are not justified here.

This integrated interpretation is the appropriate place for the ML novelty. The value is not algorithmic complexity, but disciplined calibration governance: raw DPV data are cleaned, modelled, cross-validated and assessed in a way that makes overfitting visible. For laboratory electrochemical studies with small datasets, this is more defensible than presenting nonlinear ML as inherently

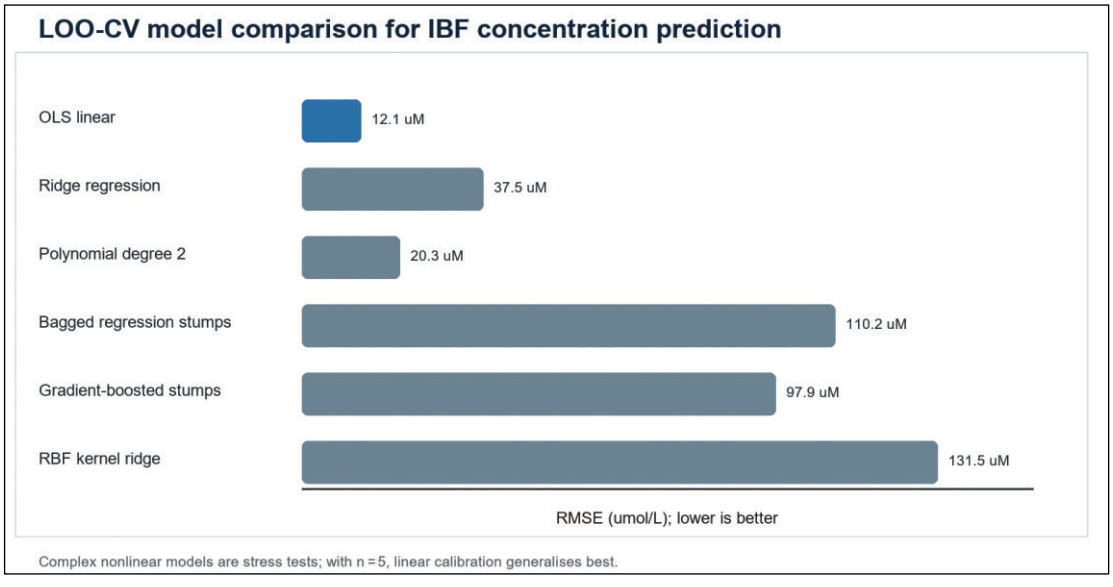

Fig. 6. Leave-one-out cross-validation model comparison. OLS inverse calibration gave the lowest RMSE, whereas nonlinear models showed higher prediction errors under the five-point calibration constraint

superior. The workflow identifies the model justified by the available evidence and makes the calibration decision reproducible.

More specifically, the model comparison provides three pieces of analytical information that the conventional calibration statistics alone do not. First, it converts the apparent goodness of fit into a realistic, validation-based prediction uncertainty: although the calibration line gives $R^2 = 0.9970$, the leave-one-out analysis shows that a concentration predicted for an unseen sample carries an expected error of approximately 12 μM, RMSE, corresponding to about 2.5–12% of the analyte concentration across the working range. This held-out error, rather than the calibration line's fit statistics, is the figure that describes how accurately the sensor predicts an unknown sample. LOO-CV gave an RMSE of 12.11 μM for the OLS inverse-calibration model. This value represents the average prediction error when each calibration point is predicted from a model trained on the remaining four points. Expressed relative to the calibration range (100–488 μM), the RMSE corresponds to 3.12% of the full range or approximately 4.10% of the mean concentration (295.6 μM). These results indicate that the prediction error is small relative to the working concentration interval, supporting the suitability of the linear calibration model for the investigated concentration range. The comparison, therefore, turns the usual qualitative warning against overfitting small electrochemical datasets into measured numbers that can guide method development in other laboratories. Third, the OLS LOO-CV error establishes a quantitative benchmark for future model development: any more complex calibration approach – for example, multivariate models using the entire voltammogram as input, or matrix-corrected models intended to compensate for the signal suppression observed in tap water (Section 'Selectivity and interference study'), must outperform this 12.11 μM reference error before its added complexity is justified. The machine-learning comparison is thus reported not as a demonstration of algorithmic superiority, but as a documented negative result and a transferable model-selection protocol for the small-sample electroanalysis.

CONCLUSIONS

A Gr-Chit/GCE was developed as a simple DPV platform for IBF screening and paired with an explicit calibration-validation workflow. The modification increased the effective electroactive area, shifted the IBF oxidation potential slightly lower, and produced a linear response from 100 to 488 μM. The recalculated figures of merit were sensitivity = 0.0275 μA μM^{-1}, $R^2 = 0.9970$, LOD = 22.27 μM and LOQ = 74.25 μM. Interference tests showed that AA was resolved at a lower potential, while ACT contributed in the IBF region without masking the analyte response under the tested conditions. The ML analysis strengthened the calibration claim by showing, under LOO-CV, that the OLS inverse calibration outperformed more complex models for this small, near-linear dataset. Beyond confirming linear calibration, the LOO-CV comparison provided a validation-based estimate of the concentration-prediction uncertainty (RMSE = 12.11 μM), quantified the penalty for an unjustified model complexity, and set a reference error that future multivariate or matrix-corrected calibration models must surpass. Overall, the manuscript presents a low-cost electrode modification and an auditable calibration strategy, a combination that is more credible than unsupported claims of ML superiority for small electrochemical datasets.

Received 5 June 2026
Accepted 1 July 2026

References

1. M. C. Fletcher, J. F. Spera, *Dent. Clin. North Am.*, **56(1)**, 95 (2012).
2. M. A. Flórez-Restrepo, X. López-Legarda, F. Segura-Sánchez, *Sci. Total Environ.*, **977**, 179379 (2025).
3. G. A. Ogunwole, J. A. Adeyemi, J. K. Saliu, K. E. Olorundare, *Heliyon*, **10(11)**, e31880 (2024).
4. B.-M. Ţuchiu, R.-I. Stefan-van Staden, J. F. Van Staden, *Crit. Rev. Anal. Chem.*, **54(1)**, 61 (2024).
5. I. Moro, V. Matozzo, A. Piovan, E. Moschin, F. D. Vecchia, *Environ. Toxicol. Pharmacol.*, **38(2)**, 379 (2014).
6. C. Laghlimi, A. Moutcine, A. Chtaini, et al., *ADMET DMPK*, **11(2)**, 151 (2023).
7. A. J. Bard, L. R. Faulkner, *Electrochemical Methods: Fundamentals and Applications*, 2nd edn., Wiley, New York (2001).
8. R. Navanietha Krishnaraj, R. K. Sani (eds.), *Bioelectrochemical Interface Engineering*, Wiley, Hoboken, NJ (2020).
9. Q.-L. Zhao, Z.-L. Zhang, L. Bao, D.-W. Pang, *Electrochem. Commun.*, **10(2)**, 181 (2008).

10. C. E. Banks, R. G. Compton, *Analyst*, **131(1)**, 15 (2006).
11. R. L. McCreery, *Chem. Rev.*, **108(7)**, 2646 (2008).
12. E. Chiavazza, S. Berto, A. Giacomino, et al., *Electrochim. Acta*, **192**, 139 (2016).
13. F. Quddus, A. Shah, N. Ullah, I. Shah, *Nanomaterials*, **14(7)**, 630 (2024).
14. A. Dehghani, S. M. Lashgari, B. Ramezanzadeh, in: *Innovations in Graphene-Based Polymer Composites*, Elsevier (2022).
15. A. V. Bounegru, I. Bounegru, *Polymers*, **15(17)**, 3539 (2023).
16. L. Naidoo, G. E. Uwaya, K. Bisetty, *Adv. Mater. Interfaces*, **12(8)**, 2400780 (2025).
17. Y. Luo, J. Liu, X. Zhang, Z. Li, *J. Electrochem. Soc.*, **169(1)**, 016502 (2022).
18. A. Hardiansyah, R. F. Maulana, N. L. W. Septiani, et al., *Carbohydr. Polym.*, **382**, 125245 (2026).
19. R. H. O. Montes, R. M. Dornellas, G. R. Salazar-Banda, M. C. Santos, *J. Electroanal. Chem.*, **775**, 342 (2016).
20. Ľ. Švorc, I. Strežová, K. Kianičková, D. M. Stanković, P. Otřísal, A. Samphao, *J. Electroanal. Chem.*, **822**, 144 (2018).
21. P. Puthongkham, S. Wirojsaengthong, A. Suea-Ngam, *Analyst*, **146(21)**, 6351 (2021).
22. K. Kaewket, T. C. R. Outrequin, S. Deepaisarn, J. Wijitsak, P. Sunon, K. Ngamchuea, *ACS Sens.*, **10(5)**, 3471 (2025).
23. R. M. Dashtaki, S. M. Dashtaki, E. Heydari-Bafrooei, M. J. Piran, *ACS Sens.*, **10(4)**, 3123 (2025).
24. P. Király, G. Tóth, *J. Chemom.*, **39(4)**, e70026 (2025).
25. A. Vabalas, E. Gowen, E. Poliakoff, A. J. Casson, *PLoS One*, **14(11)**, e0224365 (2019).
26. E. Sramkova, T. Bystron, K. Bouzek, *Electrochim. Acta*, **379**, 138177 (2021).
27. I. Yasmin, M. I. Kanjal, U. Sattar, et al., *J. Chem. Soc. Pak.*, **47(6)**, 517 (2025).
28. S. Amin, M. T. Soomro, N. Memon, et al., *Environ. Nanotechnol. Monit. Manag.*, **1–2**, 8 (2014).
29. N. Dondo, M. Shumba, M. Moyo, S. Nyoni, *Arab. J. Chem.*, **13(11)**, 7809 (2020).
30. M. Roushani, F. Shahdost-fard, *Mater. Sci. Eng.* C, **68**, 128 (2016).
31. M. Roushani, F. Shahdost-fard, *Mater. Sci. Eng.* C, **75**, 1091 (2017).
32. F. Shahdost-fard, M. Roushani, *J. Electroanal. Chem.*, **763**, 18 (2016).
33. M. Roushani, F. Shahdost-fard, *Bioelectrochemistry*, **126**, 38 (2019).

Islam Hassan, Mohamed Abdelkader, Rasa Pauliukaitė

IBUPROFENO ELEKTROCHEMINIS APTIKIMAS ANT GRAFENO IR CHITOZANO MODIFIKUOTO STIKLINIO ANGLIES ELEKTRODO: DIFERENCINĖS IMPULSINĖS VOLTAMPEROMETRIJOS INTEGRAVIMAS SU MAŠININIO MOKYMOSI KALIBRAVIMU